nature communications

Article

https://doi.org/10.1038/s41467-024-53587-6

Mefloquine-induced conformational shift in Cx36 N-terminal helix leading to channel closure mediated by lipid bilayer

Received: 9 April 2024

Accepted: 15 October 2024

Published online: 25 October 2024

Check for updates

Hwa-Jin Cho, Dong Kyu Chung & Hyung Ho Lee

Connexin 36 (Cx36) forms interneuronal gap junctions, establishing electrical synapses for rapid synaptic transmission. In disease conditions, inhibiting Cx36 gap junction channels (GJCs) is beneficial, as it prevents abnormal synchronous neuronal firing and apoptotic signal propagation, mitigating seizures and progressive cell death. Here, we present cryo-electron microscopy structures of human Cx36 GJC in complex with known channel inhibitors, such as mefloquine, arachidonic acid, and 1-hexanol. Notably, these inhibitors competitively bind to the binding pocket of the N-terminal helices (NTH), inducing a conformational shift from the pore-lining NTH (PLN) state to the flexible NTH (FN) state. This leads to the obstruction of the channel pore by flat double-layer densities of lipids. These studies elucidate the molecular mechanisms of how Cx36 GJC can be modulated by inhibitors, providing valuable insights into potential therapeutic applications.

Cell-to-cell communication is a crucial process in multicellular organisms, facilitated by intercellular signaling. This communication involves the direct connection of adjacent cells, achieved by the end-to-end docking of two hexameric hemichannels (referred to as connexons) from each cell, resulting in the formation of a dodecameric gap junction channel (GJC)[1]. GJCs, which are part of the large-pore channel family that includes calcium homeostasis modulators (CALHMs) and leucine-rich repeat-containing 8 (LRRC8) channels, facilitate the direct interchange of diverse signals, including electrical impulses and various molecules like ions, second messengers, hormones, and metabolites. In particular, GJCs play pivotal roles in diverse cellular processes, including neuron electrical synchronization, development, differentiation, and immune response[1,2]. Vertebrate GJCs are formed by connexins, and there are 21 human connexin genes, which are differentially expressed depending on the tissue or cell type. For instance, while Cx43 is widely expressed in various organs, hepatocytes specifically express Cx26 and Cx32, and Cx36 is predominantly found in neurons[1].

The proper function of connexins is regulated by multiple factors, including extracellular and intracellular environments, and molecular regulators[1,3], enabling cells to promptly adjust the turnover rate, channel gating, and permeability of GJC at their membrane in response to internal and external signals[4]. Despite the structural homology among connexins, different connexin types exhibit unique properties, including permeability and selectivity[5]. Therefore, comprehending the distinctive attributes of individual connexins and elucidating their regulatory mechanisms across diverse physiological and pathological contexts holds significant importance. However, the precise molecular mechanisms governing how connexins are regulated by intracellular and extracellular factors remain elusive.

Connexin 36 (Cx36) is primarily found in neurons, establishing gap junctions that interconnect neighboring neurons. This molecular architecture leads to the formation of specialized junctions known as electrical synapses, facilitating the rapid transmission of electrical signals and promoting synchronous firing among interconnected neurons. The functionality of Cx36 GJC is influenced by factors such as transjunctional voltage and intracellular pH, cytosolic magnesium ion, arachidonic acid (AA), and regulator molecules like mefloquine (MFQ) and n-alkanols[6–8]. In certain pathological states such as progressive cell death and hypersynchronous neuronal activity, Cx36 GJC participates in the propagation of apoptotic signals and contributes to the occurrence of aberrant synchronous firing, as observed in seizure episodes[9–12]. Thus, the use of inhibitors

Department of Chemistry, College of Natural Sciences, Seoul National University, Seoul 08826, Korea. e-mail: hyungholee@snu.ac.kr

targeting Cx36 GJC for pharmacological purposes holds promise in potentially disrupting neuronal synchronization during seizure activity and protecting neurons[13,14], although it is important to recognize the potential for disrupting normal brain function[15,16]. Notably, it has been shown that blocking Cx36 GJC has the capability to efficiently mitigate the severity of seizures, potentially yielding antiepileptic effects[13]. Despite the importance of Cx36 channel inhibition, the mechanism underlying Cx36 channel inhibition remains elusive.

Recently, we resolved the cryo-electron microscopy (cryo-EM) structures of human Cx36 GJC, unveiling a dynamic equilibrium between its closed and open states[17]. During the process of channel gating, both the N-terminal helices (NTH) and lipid molecules simultaneously play an essential role[17]. In the closed state, the channel pores are filled with two layers of lipids, and the NTHs of Cx36 are dissociated from the pore, forming a flexible NTH (FN) state. Conversely, in the pore-lining NTH (PLN) state, the channel pore is completely open without any obstruction. Given that both PLN and FN states were observed from a single grid sample, an equilibrium of conformational dynamics exists between the closed and open states, which would be modulated by intracellular or extracellular molecules.

Interestingly, small molecules such as MFQ, fatty acids like AA, carbenoxolone, and n-alkanol were known to block Cx36 GJC[1,18,19]. Among them, MFQ, an FDA-approved antimalarial compound, is used for the prevention or treatment of mild and moderate malaria[20], with neuropsychiatric side effects including depression, anxiety, vivid dreams, hallucinations, and psychosis due to its action on the central nervous system[14,18,21]. Later, it was discovered that MFQ specifically blocks Cx36 GJC, contributing to these side effects. Moreover, it offers neuroprotective effects in certain disease conditions such as spreading depression, NMDAR-mediated neuronal death, tremor, motor deficits, convulsants, stage IV seizures, cell death upon oxygen-glucose deprivation, and hypersensitivity to pain[22–29]. Additionally, it is noteworthy that MFQ exhibits 10- to 100-fold higher sensitivity to Cx36 (IC_{50} value of 310 nM) and Cx50 (IC_{50} value of 1.1 μM) compared to other connexins. Thus, the Cx36-specific channel inhibitor MFQ is regarded as a valuable tool for investigating the regulation mechanism of Cx36 GJC[18]. Another Cx36 GJC inhibitor, AA, is an endogenous non-specific channel inhibitor of connexins[7,30]. Under physiological conditions, only a small fraction of Cx36 GJCs, which are assembled into junctional plaques, remain open. However, the number of fractional channels and junctional conductance undergo a significant increase when endogenous AA levels are reduced through exposure to fatty acid-free bovine serum albumin or cytosolic phospholipase A2 inhibitors[7].

In this study, we elucidate cryo-electron microscopy structures of human Cx36 GJC in complex with its channel modulators like MFQ, AA, and 1-hexanol. Notably, these hydrophobic molecules competitively bind to a hydrophobic groove (H.G.) formed by TM1 and TM2, where NTH binds in its open state (PLN state), shifting the conformational dynamic equilibrium of NTHs towards the closed state (FN state). These studies elucidate the previously unresolved molecular mechanisms of how Cx36 GJC can be modulated by inhibitors, providing valuable insights into potential therapeutic applications.

Results

Structural features of Cx36 GJC in nanodiscs containing brain lipids

To investigate the distinctive structural characteristics of Cx36 GJC in complex with its inhibitors compared to apo Cx36 GJC, we aimed to reconstitute Cx36 GJC within a lipid nanodisc composed of porcine brain total lipid extracts ($Cx36_{Nano\text{-}BL}$-WT), considering that Cx36 functions in neuronal GJC. The details of the cryo-EM structures determined in this study are summarized in Fig. 1a. As a first step, we determined the cryo-EM structure of human Cx36 in lipid nanodiscs containing brain lipids (Supplementary Fig. 1). This necessity arose from the impact of lipid composition on NTH conformation of Cx36 and the absence of an available 3D structure for apo Cx36 GJC reconstructed in brain lipids[17]. The structures of $Cx36_{Nano\text{-}BL}$-WT showed both PLN and flexible N-terminal helix (FN) states (Supplementary Fig. 1), similar to those solved in a lipid nanodisc containing soybean lipids ($Cx36_{Nano\text{-}SL}$-WT, Supplementary Fig. 2b). When overall structures were superimposed, both structures aligned well with identical structural features, including the loose NTH-TM1 loop, the α-to-π-transition of TM1, and the hydrophobic pocket at the channel entrance (Supplementary Fig. 2b, c). However, protomer-focused 3D classification (see method for detail) on $Cx36_{Nano\text{-}BL}$-WT revealed that the ratio of Cx36 protomers in the PLN state and the FN state was approximately 3:7 (Supplementary Fig. 3a, b), in contrast to the previously reported 6:4 ratio for $Cx36_{Nano\text{-}SL}$-WT[17]. These observations suggest a subtle distinction in the conformational dynamic equilibrium contingent upon the phospholipid composition of the nanodisc.

MFQ or AA binding induces a conformational change of NTH in Cx36

Chemical inhibitors, such as MFQ and AA, are widely acknowledged to induce a fully closed state of the Cx36 GJC[1,7,18]. To explore the molecular mechanism underlying the inhibition of Cx36 GJC by MFQ and AA, we elucidated the cryo-EM structures of Cx36 in complex with MFQ ($Cx36_{Nano\text{-}BL}$-MFQ) or AA ($Cx36_{Nano\text{-}BL}$-AA) in a lipid nanodisc containing brain lipids at resolutions of 2.7 Å and 3.0 Å, respectively (Fig. 1). Both complex structures exhibited the full FN conformation and displayed similar overall structures to the previously determined Cx36 GJC structures in the FN state, reconstituted in soybean lipids (Supplementary Fig. 2b–d)[17]. Notably, both MFQ and AA bind to the H.G., the highly hydrophobic region within the channel pore (Fig. 1b, c), which is formed by hydrophobic residues from TM1 and TM2 (Fig. 1b, c, upper boxes). While investigating the inhibition mechanism of Cx36 by MFQ and AA, the Cx36-MFQ complex and the Cx32-MFQ complex in detergent micelles were recently reported, showing only the FN state, both in the presence and absence of MFQ[31,32]. This observation aligns with our previously determined structures of human Cx36 in detergents[17], suggesting that detergents significantly influence the conformation equilibrium between the PLN and FN states.

When we measured the water-accessible pore diameters of both structures ($Cx36_{Nano\text{-}BL}$-MFQ and $Cx36_{Nano\text{-}BL}$-AA), they were ~12 Å at their narrowest points (Fig. 1b, c, bottom boxes). The binding of MFQ and AA resulted in a reduction of the pore size at the binding site from ~21 Å to ~13 Å, indicating a decrease of approximately 8 Å (Fig. 1d, yellow dashed line and green and purple solid lines). However, their bindings were insufficient to entirely obstruct the channel pore (Fig. 1b, c, bottom boxes). This is in line with the inherent characteristics of the relatively large pore size of Cx36, preventing the direct blockage of the channel pore by the inhibitors. Upon removal of the inhibitors from the atomic models of $Cx36_{Nano\text{-}BL}$-MFQ and $Cx36_{Nano\text{-}BL}$-AA, the channel pore size closely aligned with that of the previously established Cx36 structure in the FN state (Supplementary Fig. 2d, e). Furthermore, the characteristic α-helix or π-helix structural features observed in previous Cx36 GJC structures in PLN and FN states were also evident at residues 30-VVIF-33 of TM1 in both $Cx36_{Nano\text{-}BL}$-MFQ and $Cx36_{Nano\text{-}BL}$-AA (Supplementary Fig. 2c). Taken together, we concluded that the binding of MFQ and AA to the Cx36 GJC does not directly obstruct the pore, but it induces a conformational change of NTH into the FN state, corresponding to the closed state.

The competitive binding of MFQ or AA to the H.G. induces the FN state of NTH

We then examined the binding site of MFQ and AA, which is located within the hydrophobic groove of Cx36. This groove is shaped by hydrophobic residues from TM1 (Ile35, Val38, and Ala39) and TM2 (Val80, Ile83, and Ile84) at the interface of the channel entrance and pore (Fig. 2b, c). In the $Cx36_{Nano\text{-}BL}$-WT (FN state), weakly disordered densities indicative of membrane components surround the hydrophobic groove within the channel pore. However, in both $Cx36_{Nano\text{-}BL}$-MFQ and $Cx36_{Nano\text{-}BL}$-AA, clearly ordered densities corresponding to MFQ or AA emerge (Fig. 2b, c).

Remarkably, both MFQ and AA competitively bind to the H.G. region, the binding pocket of the NTHs. Upon superimposing the structures of $Cx36_{Nano\text{-}BL}$-MFQ and $Cx36_{Nano\text{-}BL}$-AA onto $Cx36_{Nano\text{-}BL}$-WT, Trp4 of NTH in $Cx36_{Nano\text{-}BL}$-WT precisely aligns with MFQ and AA of $Cx36_{Nano\text{-}BL}$-MFQ and $Cx36_{Nano\text{-}BL}$-AA, respectively (Fig. 2d). The binding characteristics suggest that both MFQ and AA bind to the H.G. more effectively than Trp4, i.e., both molecules present broader binding surfaces to the H.G. than Trp4 (Fig. 2), making MFQ and AA more adept at interacting with the H.G. Consequently, the competitive binding of MFQ or AA to the H.G. of Cx36 GJC might prevent Trp4 binding, ultimately triggering the FN state.

To assess the impact of MFQ and AA on the conformational equilibrium of Cx36 GJC, we performed protomer-focused 3D classification following the methodology detailed in our previous work[17]. Strikingly, both inhibitor-bound structures exclusively exhibited FN protomers, with no observation of PLN protomers (Fig. 3). In the absence of inhibitors, the ratio of PLN to FN protomers was approximately 3:7. However, upon the binding of inhibitors, the ratio completely shifted towards FN protomers (Fig. 3). Essentially, the binding of MFQ or AA to the H.G., displacing Trp4, triggers a transition in the conformational dynamic equilibrium towards the FN state. Overall,

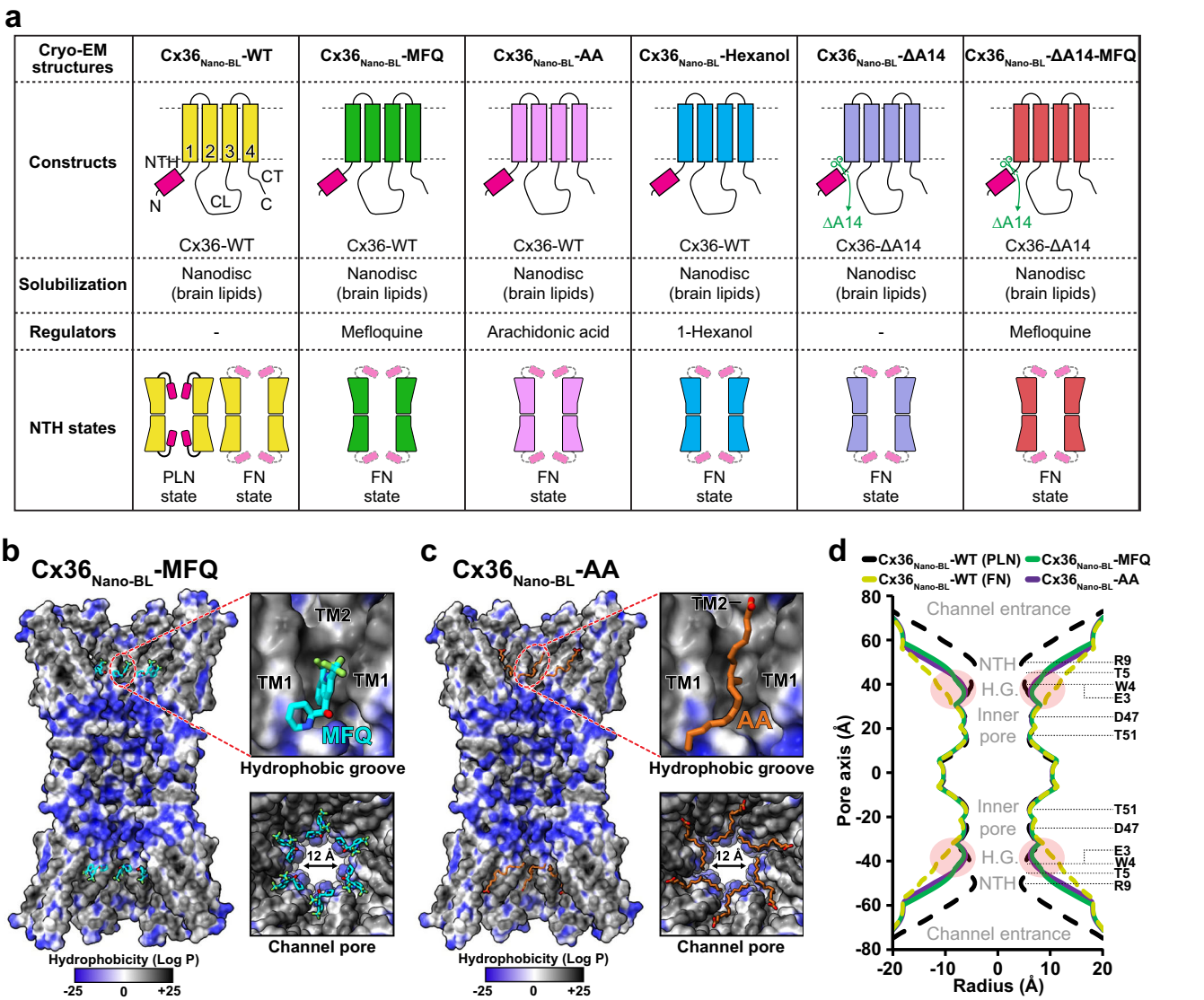

Fig. 1 | Cryo-EM structures of human Cx36 in complex with mefloquine and arachidonic acid. a A schematic diagram summarizing the seven cryo-EM structures of human Cx36 in this study, including the nomenclature used. **b**, **c** Cryo-EM maps representing surface hydrophobicity of $Cx36_{Nano\text{-}BL}$-MFQ and $Cx36_{Nano\text{-}BL}$-AA in cross-sectioned side view. The upper and bottom boxes present close-ups of the hydrophobic groove and a top view, respectively. The water-accessible pore diameter is indicated in the bottom boxes. The surface hydrophobicity (Log P) of atomic models is computed and visualized using UCSF ChimeraX[61], where hydrophobic and hydrophilic surfaces are color-coded in a gradient of dark gray and blue. The channel pore-bound MFQ and AA are depicted in cyan and brown sticks, respectively. **d** A comparison of the water-accessible pore diameter of Cx36 GJC structures is shown. $Cx36_{Nano\text{-}BL}$-WT in PLN and FN states are colored in black and yellow dashed lines, while $Cx36_{Nano\text{-}BL}$-MFQ and $Cx36_{Nano\text{-}BL}$-AA are colored in green and purple solid lines, respectively. Source data are provided as a Source Data file.

https://doi.org/10.1038/s41467-024-53587-6

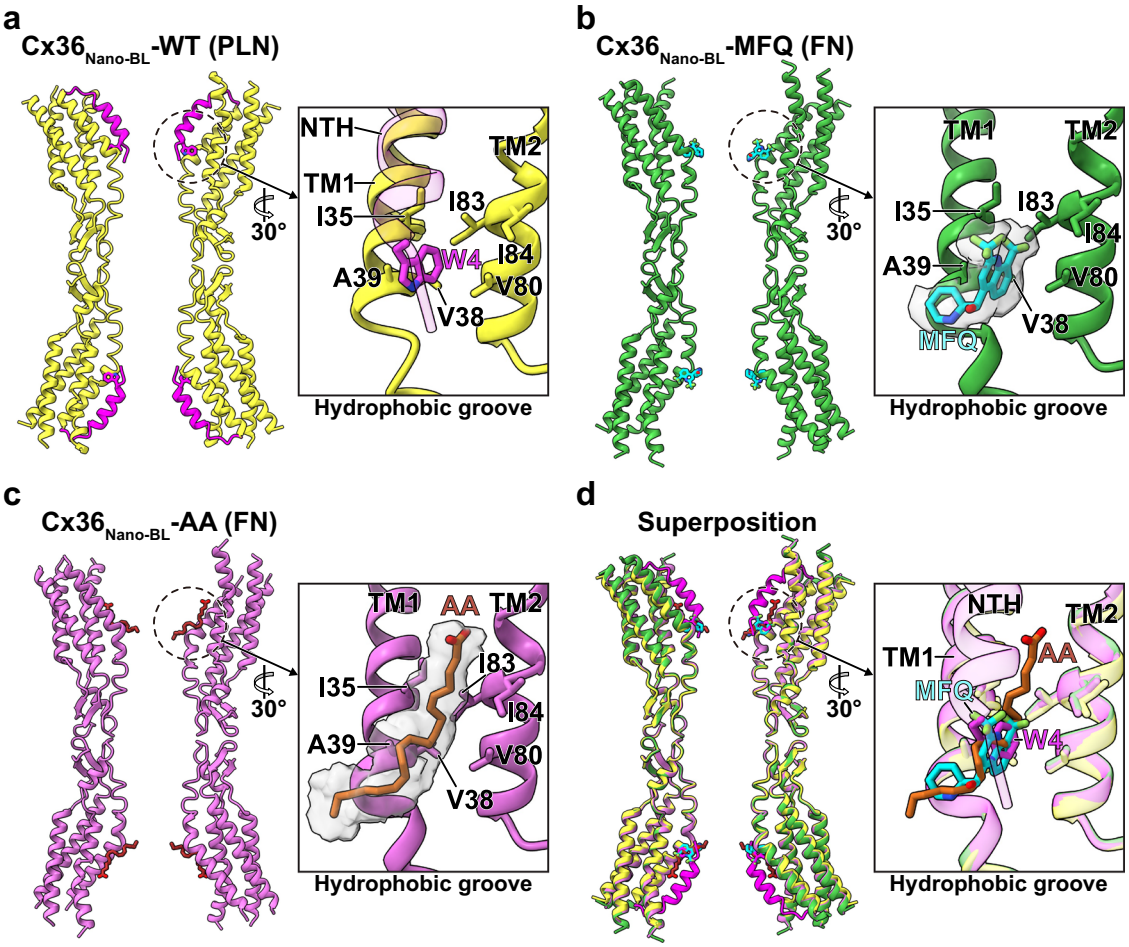

Fig. 2 | Common hydrophobic binding site of MFQ and AA in Cx36 GJC. a–d The ribbon representation of $Cx36_{Nano\text{-}BL}$-WT in PLN (**a** yellow ribbon), $Cx36_{Nano\text{-}BL}$-MFQ (**b** green ribbon), $Cx36_{Nano\text{-}BL}$-AA (**c** pink ribbon), and their superimposition (**d**). The close-up of the H.G. is presented in boxes. The H.G. is composed of hydrophobic residues from TM1 (Ile35, Val38, and Ala39) and TM2 (Val80, Ile83, and Ile84). The NTH and Trp4 of $Cx36_{Nano\text{-}BL}$-WT in PLN are colored in magenta. H.G.-bound MFQ and AA, along with their coulomb density maps, are shown in cyan, brown, and gray, respectively. H.G. hydrophobic groove, NTH N-terminal helix, PLN pore-lining NTH, FN flexible NTH, MFQ mefloquine, AA arachidonic acid.

these findings suggest that MFQ and AA inhibit Cx36 GJC by inducing a conformational shift from the PLN state to the FN state through competitive bindings to the H.G. within the channel pore.

Lipid-mediated occlusion in inhibitor-bound Cx36 GJC structures

In our previous study, we demonstrated a correlation between the NTH conformation (PLN or FN states) and channel gating by lipids[17]. The channel pores of Cx36 GJC are filled with two layers of lipids in the pore-occluded state, with the NTHs dissociated from the pore. Conversely, the channel pore is completely open without any obstruction in the PLN state. This suggests that the binding and dissociation of NTHs to the hydrophobic groove are critical steps in regulating channel gating, although the mechanism by which the conformational equilibrium of NTHs is regulated remains unknown.

Similarly, we observed double-layer density maps in $Cx36_{Nano\text{-}BL}$-MFQ and $Cx36_{Nano\text{-}BL}$-AA, completely occluding the channel pore (Fig. 3b, c). To avoid artifacts from D6 symmetry imposition during 3D reconstruction, we reconstructed the density maps without imposed symmetry (C1 symmetry). These two layers correspond to the cytoplasmic layer (C.L.), and extracellular layer (E.L.) (Fig. 3). The densities associated with MFQ and AA are located in the E.L. (Fig. 3b, c, cyan and brown densities). While the channel pore was not completely obstructed by the binding of MFQ or AA alone, as demonstrated in Fig. 1, it is fully occluded by the disordered densities (Fig. 3b, c). As elucidated in our prior study, these layers are attributed to lipids, as we excluded the possibility of self-occlusion by components of Cx36 GJC, including NTH, cytoplasmic loop, and C-terminal tail[17]. Moreover, the features of the pore-obstructing densities, including double layers, flatness, and a thickness of ~4 nm in $Cx36_{Nano\text{-}BL}$-MFQ and $Cx36_{Nano\text{-}BL}$-AA are highly consistent with those of innexin-6 (INX6) hemichannel and pannexin 1 (PANX1) channel[33,34], suggesting a common mechanism of channel pore occlusion by lipids. Taken together, our structures reveal that the occlusion of the Cx36 channel pore by lipids can be induced by the binding of MFQ or AA.

The lipid-mediated channel occlusion was initially proposed based on structural studies of the calcium homeostasis modulator 2 (CALHM2) channel and was later observed in INX6, LRRC8C, PANX1, Cx36, and connexin 43 (Cx43) channels[33–38]. Although the solvent-accessible pore sizes vary among these channels: CALHM2 (60 Å), INX6 (16 Å), LRRC8C-8A chimera (4.7 Å), PANX1 (17 Å), Cx36 (12 Å), and Cx43 (10 Å)[33–37], the lipid-plugging mechanism for channel closure has been repeatedly proposed in the large-pore channel family. The LRRC8 channel exhibits pore-plugging double-layered densities in both detergent micelles and lipid nanodiscs and has a disordered N-terminus similar to Cx36[37]. The N-terminus of PANX1 is also detached from the transmembrane domain by the addition of probenecid, a channel inhibitor, leading to lipid-mediated double-layered pore occlusion[34]. Similarly, 1-palmitoyl-2-oleoyl-phosphatidylethanolamine and cholesteryl hemisuccinate (CHS) bind to the hydrophobic

https://doi.org/10.1038/s41467-024-53587-6

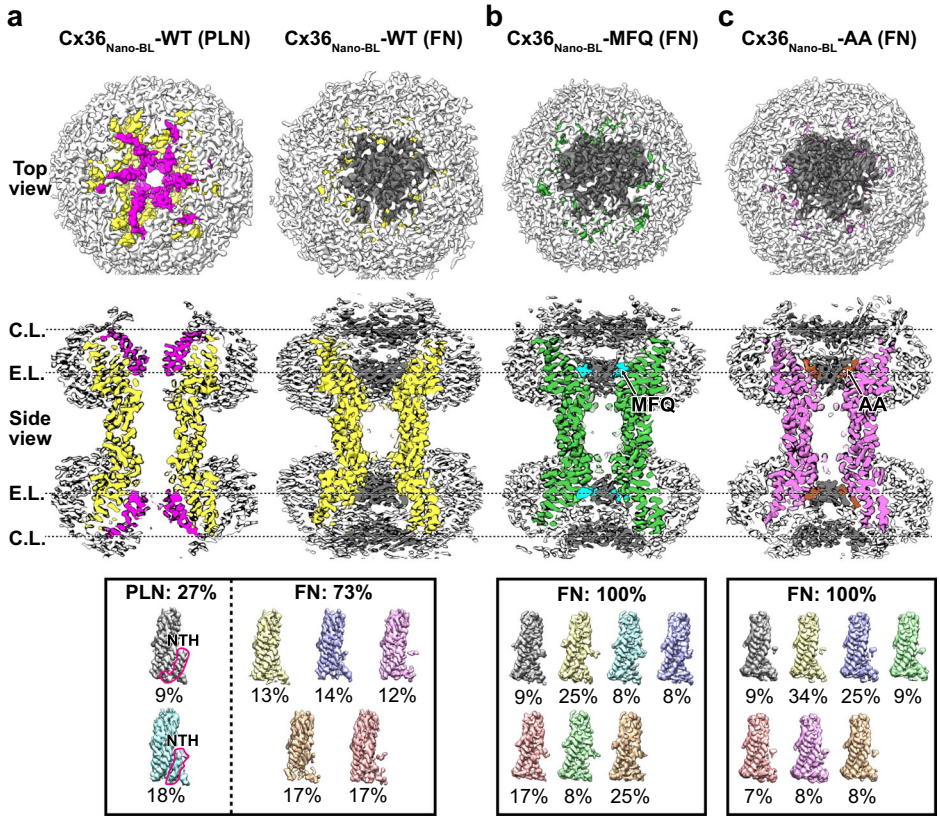

Fig. 3 | Structural characterization of the pore-occluded states of $Cx36_{Nano\text{-}BL}$-MFQ and $Cx36_{Nano\text{-}BL}$-AA in lipid nanodiscs. a–c Top and cross-sectioned side views of the cryo-EM reconstruction map with C1 symmetry imposition. The densities of $Cx36_{Nano\text{-}BL}$-WT in PLN and FN states (**a**) are displayed in yellow, while $Cx36_{Nano\text{-}BL}$-MFQ (**b**) and $Cx36_{Nano\text{-}BL}$-AA (**c**) are displayed in green and pink, respectively. The NTHs and double-layered pore-occluding lipids at the C.L. and E.L. are highlighted in magenta and dark gray, respectively. The hydrophobic groove (H.G.)-bound MFQ and AA, as well as lipid nanodiscs, are shown in cyan, brown, and white, respectively. The summary of the protomer-focused 3D classification of $Cx36_{Nano\text{-}BL}$-WT, $Cx36_{Nano\text{-}BL}$-MFQ, and $Cx36_{Nano\text{-}BL}$-AA is viewed in the bottom boxes. NTH N-terminal helix, PLN pore-lining NTH, FN flexible NTH, MFQ mefloquine, AA arachidonic acid, C.L. cytoplasmic layer, E.L. extracellular layer.

surface in the channel pore of Cx43 GJC reconstituted in lipid nanodiscs and stabilize the gate-covering NTH (GCN) conformation. In the GCN conformation, Cx43 exhibits disordered pore-occluding densities of phospholipids and CHS at the extracellular end of the channel pore, corresponding to the extracellular layer in Cx36[35].

Hexanol-driven incomplete occlusion of the channel pore

Next, we hypothesized that a weaker regulator, compared to MFQ and AA, might lead to incomplete occlusion of the Cx36 channel pore, as it could potentially fail to induce a complete shift in the NTH conformation from PLN to FN states. Previous electrophysiological investigations on Cx36 GJC revealed a decrease in channel conductance upon exposure to various alkanols[7]. The n-alkanols are hydrophobic molecules, with hydrophobicity increasing based on the carbon chain length. For instance, 1-hexanol has a hydrophobicity (Log P) of 1.83, while 1-heptanol through 1-decanol exhibits higher hydrophobicity values ranging from 2.31 to 3.44[39]. Additionally, it is recognized that n-alkanols with different carbon chain lengths have distinct effects on Cx36[39,40]. This observation prompted us to consider that the introduction of such a short alkanol, 1-hexanol, could potentially induce an incomplete shift in the conformational equilibrium of Cx36 GJC towards the PLN state. To test this hypothesis, we determined the cryo-EM structure of Cx36 in the presence of 1-hexanol ($Cx36_{Nano\text{-}BL}$-Hexanol) at a resolution of 3.2 Å (Supplementary Fig. 2a).

Indeed, we observed density maps presumed to correspond to 1-hexanol at the hydrophobic groove (Supplementary Fig. 2a), and the binding site of 1-hexanol corresponds to those of MFQ, AA, and Trp4 of NTH within the H.G. (Supplementary Fig. 2b). When we reconstructed the density maps of $Cx36_{Nano\text{-}BL}$-Hexanol without symmetry imposition (C1 symmetry), consistent with $Cx36_{Nano\text{-}BL}$-MFQ and $Cx36_{Nano\text{-}BL}$-AA, the double-layer densities corresponding to the C.L. and E.L. are significantly weakened, displaying incomplete occlusion (Supplementary Fig. 4c–e). Consequently, we concluded that 1-hexanol, similar to MFQ and AA, can induce the conformational change of NTH toward the FN state through competitive bindings to the H.G. within the channel pore, but it does not result in complete channel occlusion. Taken together, the structural features of $Cx36_{Nano\text{-}BL}$-Hexanol suggest that pore occlusion by lipids can be modulated by various inhibitors depending on their capability to remove NTH through competitive bindings to the H.G.

The preferred binding of MFQ to the H.G. in the PLN state of NTH

We next investigated the potential contribution of the conformational state of NTH to MFQ binding. Since the binding of MFQ to the H.G. is associated with the conformational transition of NTH from PLN to FN states, we postulated that MFQ could bind to the H.G. of Cx36 when NTH is in the PLN state. To test this hypothesis, it was imperative to generate a mutant in which the conformational equilibrium of NTH is entirely shifted to the FN state. During our mutational exploration around the NTH, we uncovered an intriguing variant, Cx36 Ala14 deletion ($Cx36_{Nano\text{-}BL}$-ΔA14), demonstrating a complete FN state (Supplementary Fig. 3b). This observation suggested that the Ala14 deletion facilitated the FN state of NTH while the channel pore was obstructed by lipid double layers (Fig. 4c). Although the reason for the impact of Ala14 deletion on the NTH conformation of Cx36 remains unclear, this variant

https://doi.org/10.1038/s41467-024-53587-6

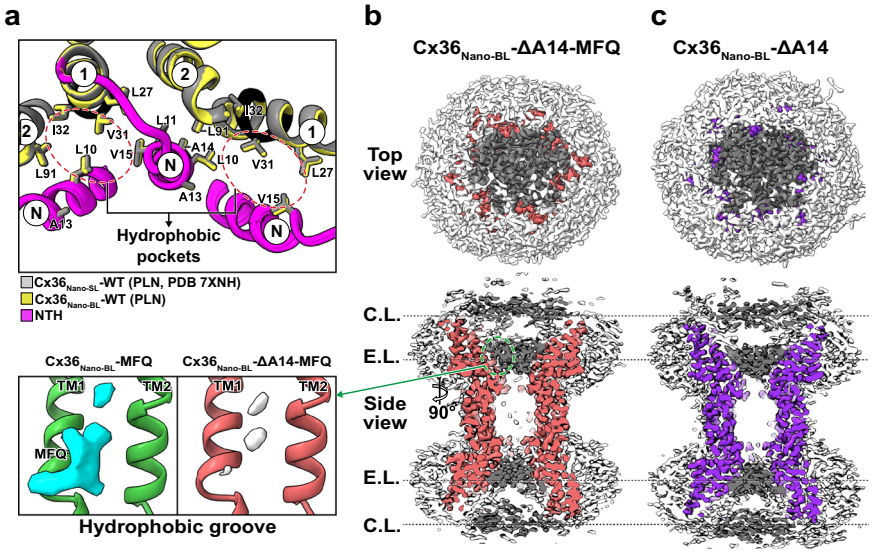

Fig. 4 | The unfavorable binding of MFQ to the H.G. in the FN state of NTH of Cx36 in lipid nanodiscs. a Structural comparison around the hydrophobic pocket of $Cx36_{Nano\text{-}BL}$-WT (yellow) with the PLN state and the previously determined structure of Cx36-WT in soybean lipids ($Cx36_{Nano\text{-}SL}$-WT, gray)[17]. The NTH is colored in magenta. The circled N, 1, and 2 denote NTH, TM1, and TM2, respectively. **b**, **c** Top and cross-sectioned side views of the cryo-EM reconstruction map with C1 symmetry imposition. The GJC densities of $Cx36_{Nano\text{-}BL}$-ΔA14-MFQ (**b**) and $Cx36_{Nano\text{-}BL}$-ΔA14 (**c**) are displayed in dark red and purple, respectively. The double-layered pore-occluding lipids at the C.L. and E.L. and lipid nanodiscs are colored dark gray and white, respectively. The close-ups of H.G. of $Cx36_{Nano\text{-}BL}$-MFQ and $Cx36_{Nano\text{-}BL}$-ΔA14-MFQ are presented in boxes. The ribbon representation of $Cx36_{Nano\text{-}BL}$-MFQ and $Cx36_{Nano\text{-}BL}$-ΔA14-MFQ GJC, and their additional densities at H.G. are colored in green, salmon, cyan, and white, respectively. The additional densities are contoured at 4 σ.

proved valuable in representing a Cx36 with NTH in the full FN state. Moreover, it is consistent with the reduced cell-to-cell connectivity in human embryonic kidney (HEK293T) cells caused by the ectopic expression of Cx36-ΔA14, as observed in our scrape loading-dye transfer (SL-DT) assay (Supplementary Fig. 5). Despite the lower channel conductance and open probability of Cx36 compared to other connexins, resulting in relatively weaker propagation of cationic fluorescence tracer, the ectopic expression of Cx36-WT significantly enhanced the propagation of the fluorescence tracer in comparison to HEK293T cells alone[41,42]. In contrast, the expression of Cx36-ΔA14 resulted in reduced propagation of the fluorescence dye compared to Cx36-WT, remaining at a similarly low level as observed in HEK293T cells alone.

Subsequently, we determined the cryo-EM structure of the Cx36 Ala14-deletion variant in the presence of MFQ ($Cx36_{Nano\text{-}BL}$-ΔA14-MFQ) to assess whether MFQ could bind to the $Cx36_{Nano\text{-}BL}$-ΔA14 variant. Remarkably, the MFQ density map disappeared, indicating that MFQ could not bind to the H.G. of Cx36, and thereby supporting the notion that the PLN state of NTH is necessary for MFQ binding (Fig. 4).

We reasoned that MFQ may not bind to the H.G. of the $Cx36_{Nano\text{-}BL}$-ΔA14 variant in the FN state because the pore is already obstructed by lipid bilayers in the FN state, limiting MFQ's access to the H.G. (Supplementary Fig. 4g). The surface of the H.G., where Trp4 (or corresponding residues of other connexins) of NTH binds, is accessible for MFQ binding and highly structurally homologous across other connexins (Supplementary Fig. 6b)[17,35,43]. Hydrophobic residues (Ile35, Val38, Ala39, Val80, Ile83, and Ile84), which interact with MFQ, are well-conserved across connexins as hydrophobic residues (Supplementary Fig. 6a). Thus, the selectivity of MFQ binding to the H.G. depending on NTH conformation might not stem from the binding site of MFQ. Taken together, we concluded that the inability of MFQ to bind to the $Cx36_{Nano\text{-}BL}$-ΔA14 variant with the fully FN state is attributed to the pore already being obstructed by lipid double layers, preventing MFQ access to the H.G. site.

Discussion

Genetic ablation or pharmacological inhibition of neuronal connexin GJCs has been demonstrated to confer neuroprotective effects in conditions such as ischemia, traumatic brain injury, glaucoma, and amyotrophic lateral sclerosis[44–46]. Consequently, the pharmacological inhibition of neuronal connexin GJC may offer a strategy for protecting against secondary cell death in such disease contexts. Indeed, several GJC inhibitors, including MFQ, quinine, quinidine, flufenamic acid, 2-APB, and meclofenamic acid, have shown neuroprotective effects by targeting Cx36[22,46–49]. Despite its pharmacological promise and its pivotal role in disease-related neuroprotection, the molecular mechanism of Cx36 channel inhibition remains largely elusive. In this study, we utilized cryo-EM single-particle analysis to investigate the channel inhibition mechanism of human Cx36 GJC, revealing that MFQ, AA, and 1-hexanol bind to the binding pocket of NTH. It induces a conformational change from the PLN state to the FN state, leading to the obstruction of the channel pore by flat double-layer densities of lipids (Fig. 5). Intriguingly, given the inherent characteristics of the relatively large-pore size of Cx36, MFQ itself cannot plug the channel pore directly but indirectly induces the conformational changes of NTH, which are coupled with the pore obstruction by lipid double layers (Fig. 3).

With the double-layer densities at the channel pore of Cx36, tightly bound lipid molecules outside the transmembrane domain have also been identified in our cryo-EM structures, potentially affecting the channel function. These tightly bound lipids of Cx36 are present irrespective of protein conformation, lipid composition, and the presence of inhibitors (Supplementary Fig. 7a–d, bottom boxes), similar to Cx46/50 GJC, and might contribute to structural stability by interacting with the exterior of the transmembrane domain (Supplementary Fig. 7)[17,50]. The essential role of channel-bound lipid molecules in stabilizing channel structures is commonly observed in large-pore channel families such as connexin, CALHM, PANX, INX, and LRRC8 channels[17,33,35–37,51]. Moreover, in some cases, channel-bound lipid molecules also contribute to stabilizing specific conformations of the NTH. CHS molecules bind to the channel pore of CALHM1, interacting with the NTH and transmembrane domain, thereby stabilizing the NTH-bound conformation[52]. Similarly, in the PLN state of Cx36, lipid acyl chains occupy hydrophobic pockets at the channel entrance (Fig. 4a), interacting with the hydrophobic pocket composed of the

https://doi.org/10.1038/s41467-024-53587-6

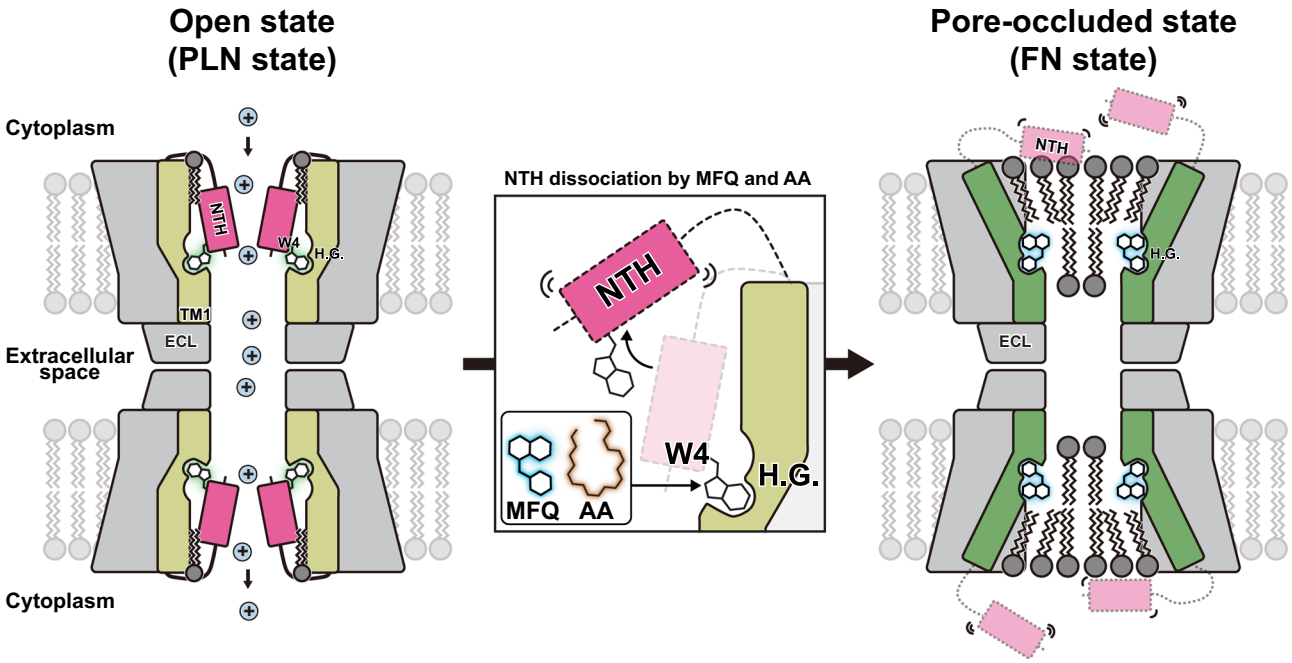

Fig. 5 | Schematic model for channel inhibition of Cx36 GJC by chemical inhibitors. Schematic representation of the open and pore-occluded states of Cx36 GJC. The NTH, TM1 in the PLN and FN states, TM2-4 and ECL1-2, lipids in the channel pore, lipid bilayer, and cation are colored magenta, yellow, green, gray, dark gray, light gray, and sky blue, respectively. Trp4 of PLN and MFQ are highlighted in green and blue, respectively. MFQ competitively binds to the H.G., where the NTH binds through Trp4. This induces a conformational change from PLN to FN state, shifting the conformational dynamic equilibrium of Cx36 GJC toward the FN state.

NTH, the NTH-TM1 loop, TM1, and TM2, suggesting their role in stabilizing the PLN state of NTH.

According to previous structural studies, various inhibitors block large-pore channels through different mechanisms. For instance, ruthenium red, an inhibitor of CALHM1 calcium channels, binds to and directly plugs the channel pore. Similarly, 4-(2-Butyl-6,7-dichloro-2-cyclopentyl-indan-1-on-5-yl)oxybutyric acid directly blocks the channel pore of LRRC8 channels[34,53,54]. In the case of PANX1, carbenoxolone binds to the extracellular pore entrance and blocks it directly. Although probenecid induces dissociation of the NTH from the PANX1 pore, leading to lipid-mediated occlusion, probenecid molecules were not observed in the density map[34]. This mechanism is similar to Cx36, where MFQ and AA bind within the H.G., competing with the NTH and inducing a conformational change from the PLN state to the FN state, facilitating lipid occlusion of the channel pore. Collectively, this comparison of channel blockage by inhibitors underscores the diverse mechanisms of inhibition in large-pore channel families.

In terms of electrophysiology, there are two gating mechanisms for connexin GJCs[55]. One is fast gating, which involves rapid transitions (<1 ms) between the open and residual states. The other is slow gating, which involves slower transitions (>10 ms) between the open state and the fully closed state[55,56]. It is generally considered that the slow gating of connexins is sensitive to factors such as transjunctional voltage, intracellular Ca^{2+}, and pH, as well as chemical inhibitors like MFQ and AA[55,56], where MFQ is classified as an inhibitor that affects the slow gating of Cx36[56–58]. In this sense, our proposed mechanism of Cx36 inhibition by MFQ provides evidence of the relationship between the H.G. and slow gating. Indeed, the binding site of MFQ consists of regions that are considered to play a role in slow gating of connexin GJCs, i.e., specific pore-lining residues, including Met34 of Cx26, Leu35, Ala39, Glu43, Gly46, and Asp51 of Cx46, and residues from Phe43 to Asp51 of Cx50, have been identified as contributors to slow gating[55,59–61]. Although a substantial body of evidence is required to fully prove the slow gating mechanism, our study suggests that the lipid-mediated Cx36 blocking by the binding of MFQ to H.G. might be partly related to the slow gating mechanism.

Fatty acids such as AA constitute a component of the cytoplasmic membrane and play a role in regulating the junctional conductance of GJCs. It was reported that AA exhibits inhibitory effects on connexin GJCs, and it is considered to be among the factors contributing to the diminished open probability of Cx36, functioning as an inhibitor[7]. Interestingly, through the structural analysis of $Cx36_{Nano\text{-}BL}$-AA, we confirmed that AA binds to the H.G., analogous to the interaction observed with MFQ. Despite difficulties posed by the weak density map, we fitted the carboxyl group of AA facing the cytosol, taking into account the arrangement of adjacent residues. It is intriguing to note that MFQ and AA share the same binding site, H.G. of Cx36, as well as the lipid-mediated blocking, suggesting that MFQ and AA share the same inhibition mechanism. Indeed, similar to the structure of $Cx36_{Nano\text{-}BL}$-MFQ, the conformational equilibrium of $Cx36_{Nano\text{-}BL}$-AA shifted toward the FN state (Supplementary Fig. 3).

It has been demonstrated that MFQ exhibits higher inhibition sensitivity to Cx36[18] compared to other connexins. One might expect that the MFQ binding site on Cx36 would be more specific, thus increasing the binding affinity of MFQ. However, the binding site of MFQ on Cx36 shows a notable degree of conservation based on the alignment of amino acid sequences across all connexins (Supplementary Fig. 6a). An alternative hypothesis is that other distinct structural features beyond the H.G. region contribute to the specificity of MFQ to Cx36, such as the loosely packed NTH conformation due to the insertion of Ala14, exclusively observed in Cx36. As a result, among currently available connexin structures in the PLN state, Cx36 exhibits relatively broader hydrophobic pockets that serve as binding sites for a hydrophobic molecule (Supplementary Fig 6c)[17]. The broader hydrophobic pocket is primarily attributed to the longer NTH-TM1 loop (residues Ala13-Ser19) owing to the insertion of Ala14 (Supplementary Fig. 6a). This hydrophobic pocket of Cx36 might contribute to the easier access of MFQ to the H.G., given that the position of the hydrophobic pocket allows it to connect the cytosolic region and the H.G. of Cx36. While this hypothesis could be corroborated through mutational analysis of the hydrophobic pocket, designing mutants poses a challenge since the mutation must not only refrain from

impacting the NTH conformation but also solely focus on diminishing the hydrophobicity of the core. This intricacy warrants further investigation in subsequent studies.

Overall, we showed that the hydrophobic groove of Cx36 serves as a common binding site for MFQ, AA, and 1-hexanol. Their interaction triggers a conformational change of NTH from the PLN state to the FN state, consequently shifting the conformational dynamic equilibrium of NTH toward the FN state. Given that the conformational shift from PLN to FN states leads to the obstruction of the channel pore by flat double-layer densities of lipids, we concluded that MFQ, AA, and 1-hexanol share a common inhibition mechanism for Cx36. This implies that the H.G. site of Cx36 might serve as a regulatory site for the NTH conformation, which can be utilized for designing an inhibitor to Cx36. It is tempting to speculate that the NTH conformation of other connexins might also be modulated by the binding of inhibitors to the H.G. site, considering the high structural homology of the H.G. in all connexins.

Methods

Expression and purification of Cx36-WT and Cx36-ΔA14 in Sf9 cells

All protein expression and purification experiments were conducted following our previously reported method[17]. The complete Cx36 gene was subcloned into the pFastBac expression vector (Invitrogen) to generate pFastBac-Cx36-WT. This construct was designed for the expression of Cx36 as a fusion protein with C-terminal FLAG tag, consisting of 8 amino acids (DYKDDDDK). The plasmid was modified to create pFastBac-Cx36-ΔA14 through the deletion of the Ala14 using PCR. The primers used for the cloning of Cx36-WT and Cx36-ΔA14 are summarized in Supplementary Table 1. The *Escherichia coli* DH10Bac strain (Gibco, cat #10361012) was transformed with pFastBac-Cx36-WT and pFastBac-Cx36-ΔA14, resulting in the production of Cx36-WT and Cx36-ΔA14 bacmids, respectively. These bacmids were then transfected into *Spodoptera frugiperda* (Sf9) cells to generate baculovirus containing the Cx36-WT and Cx36-ΔA14 expression cassette, following the manufacturer's instructions. Sf9 cells were obtained from ATCC (CRL-1711) and have been authenticated by the vendor. No further authentication was performed.

Sf9 cells were grown at 27 °C in ESF293 medium (Expression Systems), supplemented with 0.06 mg/ml penicillin G and 0.1 mg/ml streptomycin (Sigma). At 72 h post-infection, the cells underwent centrifugation at 500 × *g* for 10 min. The membrane was solubilized using buffer A [20 mM HEPES pH 7.5 and 200 mM NaCl], along with 5 mM ethylenediaminetetraacetic acid, and protease inhibitors (1 mM phenylmethylsulfonyl fluoride (PMSF), 2 μg/ml leupeptin, 2 μM pepstatin A, and 2 μM aprotinin), supplemented with 1% (w/v) lauryl maltose neopentyl glycol (LMNG, Anatrace) at 4 °C for 2 h. The insoluble fraction was removed through high-speed centrifugation at 100,000 × *g* for 1 h. Subsequently, the soluble fraction was diluted twofold with buffer A, supplemented with 0.01% LMNG, and combined with monoclonal anti-FLAG antibody agarose beads (Wako chemicals, cat #016-22784). This mixture was then incubated with gentle rotation at 4 °C for 5 h. The resin settled within the column and was washed three times with 10 column volumes (CVs) of buffer B [20 mM HEPES pH 7.5, 200 mM NaCl, 0.01% LMNG, and 0.001% cholesteryl hemisuccinate (CHS, Sigma)]. The proteins bound to resin were eluted using buffer B supplemented with 450 μg/ml FLAG peptide (Sigma) at 4 °C overnight. The resulting eluates were concentrated and further purified via size-exclusion chromatography using a Superose 6 Increase 10/300 column (Cytiva) pre-equilibrated with buffer B. Peak fractions were concentrated to approximately 6 mg/ml, flash-frozen in liquid nitrogen, and stored at −80 °C until use.

Reconstitution of Cx36-WT and Cx36-ΔA14 in lipid nanodiscs

Purified Cx36 proteins were reconstituted into nanodiscs formed by membrane scaffold protein (MSP1E1) and total brain lipids extract (Avanti) containing phosphatidylcholine, phosphatidylethanolamine, phosphatidylinositol, phosphatidylserine and phosphatidic acid. The lipid stock was prepared by removing chloroform under inert gas (N_2) and was resuspended in 5/0.5% (w/v) n-dodecyl-β-D-maltopyranoside (DDM)/CHS, resulting in a clear solution with an approximate concentration of 10 mg/ml.

The pET28a plasmid carrying the membrane scaffold protein (MSP1E1) gene was obtained from Addgene (plasmid #20062), and the MSP1E1 was expressed and purified following a previously described protocol[62]. The purified Cx36 proteins were mixed with the porcine brain total lipid extract stock (~10 mg/ml) in a molar ratio of Cx36 to lipids of 1:100. For the nanodisc reconstitution of Cx36 in complex with AA, a solution containing porcine brain total lipid extract and AA mixed at a molar ratio of 100:1 was used. These mixtures were incubated at 4 °C for 1 h. Subsequently, purified MSP1E1 protein was added to achieve a final molar ratio of Cx36:MSP1E1:lipids of 1:0.5:100. The mixtures were then gently rotated at 4 °C for 30 min. For detergent removal and protein-nanodisc reconstruction, 100 mg Bio-Beads SM2 resin (Bio-Rad, 100 mg) was added to the Cx36-lipid-MSP mixtures. After 2 h of gentle rotation, the supernatants were collected. An additional round of detergent removal was performed using 100 mg Bio-Beads SM2 resin, followed by overnight gentle rotation at 4 °C. The mixtures were then centrifuged at 10,000 × *g* for 10 min to remove insoluble particles, and the resulting supernatants were further purified via size-exclusion chromatography using a Superose 6 Increase 10/300 column pre-equilibrated with buffer A. Fractions containing Cx36 and Cx36-ΔA14 proteins reconstituted in lipid nanodiscs ($Cx36_{Nano\text{-}BL}$-WT, $Cx36_{Nano\text{-}BL}$-AA, and $Cx36_{Nano\text{-}BL}$-ΔA14) were concentrated to 3 ~ 5 mg/ml, flash-frozen in liquid nitrogen, and stored at −80 °C for EM grid preparation. Protein purity and quality were assessed by SDS-PAGE (Supplementary Fig. 8).

Cryo-EM specimen preparation and data collection

The chemical regulators of Cx36, including MFQ, AA, and 1-hexanol, were purchased from Sigma. MFQ and 1-hexanol were added to the protein at a 10-fold molar ratio relative to the Cx36 protomer, and the mixtures of Cx36 and inhibitors were incubated on ice for 20 min. AA was not added after the nanodisc reconstitution process. Four microliters of samples (4–6 mg/ml) were applied onto a negatively glow-discharged holey carbon grid (Quantifoil R1.2/1.3 Cu 300 mesh). Phenylalanine was added at a final concentration of 50 mM to enhance orientation diversity for all samples involving Cx36-WT and Cx36-ΔA14, such as $Cx36_{Nano\text{-}BL}$-WT, $Cx36_{Nano\text{-}BL}$-WT with MFQ ($Cx36_{Nano\text{-}BL}$-MFQ), AA ($Cx36_{Nano\text{-}BL}$-AA), and 1-hexanol ($Cx36_{Nano\text{-}BL}$-Hexanol), $Cx36_{Nano\text{-}BL}$-ΔA14, and $Cx36_{Nano\text{-}BL}$-ΔA14 with MFQ ($Cx36_{Nano\text{-}BL}$-ΔA14-MFQ). The grids were blotted and rapidly frozen in liquid ethane using a Vitrobot Mark IV (Thermo Fisher Scientific, USA) under conditions of 4 °C and 100% humidity. Cryo-EM images of $Cx36_{Nano\text{-}BL}$-WT, $Cx36_{Nano\text{-}BL}$-MFQ, and $Cx36_{Nano\text{-}BL}$-ΔA14 were acquired at PNU CORE research facilities (Pusan National University, Korea), Institute for Basic Science (IBS, Korea), and Institute of Membrane Proteins (IMP, Korea) using Krios G4 (TFS, USA) equipped with a BioQuantum K3 detector (Gatan Inc, USA). Additionally, cryo-EM images of $Cx36_{Nano\text{-}BL}$-AA and $Cx36_{Nano\text{-}BL}$-Hexanol were collected at the Center for Macromolecular and Cell Imaging (Seoul National University, Korea) using Glacios (TFS, USA) equipped with a Falcon 4 detector (TFS, USA). The cryo-EM images of $Cx36_{Nano\text{-}BL}$-ΔA14 were obtained at the National Center for Inter-University Research Facilities (NCIRF, Korea) using Krios G4 (TFS, USA) equipped with a Falcon 4 detector (TFS, USA). Automated data acquisition was carried out in electron counting mode using EPU software (TFS, USA).

Image processing and reconstruction

The cryo-EM image processing was performed using CryoSPARC version 4.1.2 and Relion 4.0 software tools[63,64]. For the $Cx36_{Nano\text{-}BL}$-WT dataset, 8777 movies were imported into CryoSPARC, undergoing initial steps including patch motion correction and patch CTF estimation. Subsequently, 4,506,088 particles, identified through reference-based auto-picking, were extracted into 300-pixel boxes and then binned by 2. Following three rounds of 2D classification, well-aligned classes were selected. From these, particles with side view orientations were used as references for training Topaz. Additional particles were picked, extracted, and classified through Topaz Extract, Extract from micrographs, and several rounds of 2D classification. The particles were then combined, and the duplicates were removed. After two rounds of heterogeneous refinement, the well-classified particles were re-extracted into 300-pixel boxes without binning and subjected to another round of 2D classification. A total of 201,311 particles were selected for 3D refinement with D6 symmetry, producing a consensus EM density map at a resolution of 2.6 Å. The particles were then transferred to Relion for further classification into the PLN state or FN state using the focused 3D classification method previously employed in our study[17]. The process involved 20 initial iterations with a regularization parameter (T) of 20, followed by 10 subsequent iterations with an increased T value ($T = 40$). A GJC mask covering both FN and PLN states was applied during 3D classification (Supplementary Fig. 1). The resulting four classes displayed distinct features: class 1, containing ~12% of GJC particles, exhibited clear map densities of PLNs, while NTH densities remained less defined in class 2–4, comprising ~88% of the particles. To enhance map quality, particles separated into two GJC conformations underwent separate 3D refinement procedures with D6 symmetry imposition. After sharpening, the results showed a 2.5 Å GJC map in the PLN state and a 2.9 Å GJC map in the FN state. Finally, 24,000 particles were used to generate the EM density map of $Cx36_{Nano\text{-}BL}$-WT in PLN state with D6 symmetry imposition, and 177,311 particles were used to generate the EM density map of $Cx36_{Nano\text{-}BL}$-WT in FN state with D6 symmetry.

For the $Cx36_{Nano\text{-}BL}$-MFQ dataset, 6483 movies were imported to CryoSPARC, where they underwent patch motion correction and patch CTF estimation. Subsequently, 3,760,541 particles were identified through reference-based auto-picking and extracted into 340-pixel boxes, which were then binned by 2. Additional particles with side view orientations, identified using Topaz, were also extracted into 340-pixel boxes and binned by 2. The particles were then combined, and the duplicates were removed. After three rounds of 2D classification and two rounds of heterogeneous refinement, the well-classified particles were re-extracted into 340-pixel boxes and subjected to another round of 2D classification. A total of 114,504 particles were used for 3D refinement with D6 symmetry, resulting in a consensus EM density map at a resolution of 2.7 Å. These particles were then transferred to Relion and underwent a single round of 3D classification ($K = 4$, $T = 32$). Finally, 30,596 particles were used to generate the EM density map of $Cx36_{Nano\text{-}BL}$-MFQ in FN state, with D6 symmetry imposed, at a resolution of 2.7 Å (Supplementary Fig. 9). Throughout the entire image processing workflow, the PLN state was not observed.

Similarly, the $Cx36_{Nano\text{-}BL}$-AA dataset was processed using CryoSPARC and Relion. Patch-based pre-processing, including patch motion correction and patch CTF estimation, was executed on a dataset containing 4,380 movies. From this, 1,627,296 particles were selected for extraction into 420-pixel boxes and subsequently binned by 2. Supplementary particles with side view orientations, identified using Topaz, were also extracted into 420-pixel boxes and binned by 2. Following three rounds of 2D classification and three rounds of heterogeneous refinement, the selected particles were re-extracted into 460-pixel boxes and subjected to one round of 2D classification. A total of 80,129 particles were then used for 3D refinement with D6 symmetry, resulting in a consensus EM density map at a resolution of 3.4 Å. After transferring the particles to Relion, one round of 3D classification ($K = 4$, $T = 20$) was performed, leading to the selection of 68,153 particles for generating EM density map of $Cx36_{Nano\text{-}BL}$-AA in the FN state, with D6 symmetry imposed, at a resolution of 3.0 Å. As in previous cases, the PLN state was not observed during the image processing procedure.

For the $Cx36_{Nano\text{-}BL}$-Hexanol dataset, 2400 movies were imported into CryoSPARC and underwent patch-based pre-processing. A total of 1,354,338 particles were identified through reference-based auto-picking. These particles were extracted into 220-pixel boxes and binned by 2, with additional particles in side view orientations, identified using Topaz, also extracted and binned by 2. After three rounds of 2D classification and one round of heterogeneous refinement, the well-classified particles were re-extracted into 240-pixel boxes and subjected to one round of 3D classification. Utilizing 289,951 particles, 3D refinement with D6 symmetry was performed, leading to the generation of a consensus EM density map at a resolution of 4.6 Å. After transferring these particles to Relion, one round of 3D classification ($K = 4$, $T = 20$) was conducted. Subsequently, 29,372 particles were selected to generate the EM density map of $Cx36_{Nano\text{-}BL}$-Hexanol in the FN state, with D6 symmetry imposed, at a resolution of 3.2 Å. As in previous cases, PLN state was not observed throughout the image processing procedure.

The processing of the $Cx36_{Nano\text{-}BL}$-ΔA14 dataset was carried out using the same methodology. Initially, patch-based pre-processing, including patch motion correction and patch CTF estimation, was applied to the dataset, which comprised 6313 movies. Subsequently, 3,692,234 particles were selected via reference-based auto-picking and extracted into 320-pixel boxes, which were then binned by 2. Additional particles with side view orientation, identified using Topaz, were also extracted into 320-pixel boxes and binned by 2. Following three rounds of 2D classification and two rounds of heterogeneous refinement, the well-classified particles were re-extracted into 320-pixel boxes and subjected to another round of 2D classification. A total 161,099 particles were used for 3D refinement with D6 symmetry, leading to the generation of a consensus EM density map at a resolution of 2.6 Å. These particles were then transferred to Relion and underwent a single round of 3D classification ($K = 4$, $T = 40$). Finally, 63,476 particles were used to generate the EM density map of $Cx36_{Nano\text{-}BL}$-ΔA14 in the FN state, with D6 symmetry imposed, at a resolution of 2.7 Å. Throughout the image processing, the PLN state was not observed.

The processing of the $Cx36_{Nano\text{-}BL}$-ΔA14-MFQ dataset was executed using CryoSPARC and Relion. Initially, patch-based pre-processing, including patch motion correction and patch CTF estimation, was applied to the dataset, which comprised 15,027 movies. Subsequently, 4,341,261 particles were identified through reference-based auto-picking and extracted into 360-pixel boxes, which were then binned by 2. Additional particles with side view orientation, identified using Topaz, were also extracted into 360-pixel boxes and binned by 2. After three rounds of 2D classification and two rounds of heterogeneous refinement, the well-classified particles were re-extracted into 360-pixel boxes and subjected to another round of 2D classification. A total of 379,039 particles were used for 3D refinement with D6 symmetry, leading to the generation of a consensus EM density map at a resolution of 2.5 Å. These particles were then transferred to Relion and underwent a single round of 3D classification ($K = 4$, $T = 40$). Finally, 51,406 particles were used to generate the EM density map of $Cx36_{Nano\text{-}BL}$-ΔA14-MFQ in the FN state, with D6 symmetry imposed, at a resolution of 2.6 Å. The PLN state was not observed throughout the entire image processing procedure. The local resolutions for all reconstructed maps were estimated using the local resolution estimation tool in CryoSPARC (Supplementary Fig. 10).

Protomer-focused 3D classification for the $Cx36_{Nano-BL}$-WT dataset

All protomer-focused 3D classifications were performed as previously reported[17]. For the $Cx36_{Nano-BL}$-WT dataset, the 201,311 particles used to generate the 2.6 Å consensus EM density map were transferred to Relion, where D6 symmetry expansion was conducted. Protomer particles were subtracted using a mask covering a single protomer (Supplementary Fig. 3a). These subtracted protomer particles were then subjected to focused 3D classification ($K = 8$, $T = 20$) using the protomer mask and without orientation search. In the resulting classes, the protomers showing clear NTH density were classified as the PLN state (PLN protomer), while those showing weak and disordered NTH density were classified as the FN state (FN protomer). Five classes exhibited the FN protomer, and two classes displayed the PLN protomer. This method was applied to the $Cx36_{Nano-BL}$-MFQ, $Cx36_{Nano-BL}$-AA, $Cx36_{Nano-BL}$-Hexanol, $Cx36_{Nano-BL}$-ΔA14 and $Cx36_{Nano-BL}$-ΔA14-MFQ datasets.

Model building and refinement

All structural models incorporating acyl chains and/or CHS molecules were built using the Coot program[65,66]. None of the models include CL (Ala102-Glu193) and CT (Trp277-Val321), and all models, except for the PLN state of $Cx36_{Nano-BL}$-WT, exclude NTH (Met1-His18) due to weak map density. The previously determined structures of $Cx36_{LMNG}$-BRIL (PDB 7XKT) and $Cx36_{Nano}$-WT in PLN state (PDB 7XNH) served as references for atomic modeling. The head groups of lipids could not be modeled due to weak map density. All structures were refined using phenix.real_space_refine in the PHENIX software and visualized using UCSF Chimera and UCSF ChimeraX[67–69].

SL-DT assay

The SL-DT assay was conducted according to a method previously described, with some modifications[70]. Human embryonic kidney (HEK293T) cells were cultured in Dulbecco's Modified Eagle's Medium (DMEM, Welgene, Korea) supplemented with 10% fetal bovine serum (Gibco) and 4 mM L-glutamine (Sigma) at 37 °C in a humidified 5% CO_2 atmosphere. HEK293T cells were grown to 60% confluency in 12-well plates. Cx36-WT and Cx36-ΔA14, both fused with C-terminal YFP, were expressed using BacMam system. Baculoviruses for this purpose were generated and amplified in Sf9 insect cells. After 60 h of incubation, the cells were rinsed twice with Dulbecco's Phosphate-Buffered Saline (DPBS, Sigma) before the addition of 0.02%, neurobiotin 350 tracer (MW: 573 Da, net charge: +1, excitation (Ex)/emission (Em): 346/452 nm, Vector Laboratories, USA) in DPBS. Scraping was performed using a carving tool with a straight edge. After scraping, the image was obtained twice: once at 30 s and once at 10 min post-incubation. The excess dye was removed by washing the cells twice with DPBS, and the cells were observed using EVOS fluorescence microscope (TFS, USA). Image analysis was carried out using NIH ImageJ software and macro according to the previously described method[71,72]. YFP fluorescence was detected using the GFP (Ex/Em: 470/525 nm) fluorescence detection mode, while blue fluorescence detection mode (Ex/Em: 360/447 nm) was utilized for the observation of neurobiotin 350 fluorescence. For each trial, HEK293T cells alone, and those expressing Cx36-WT or Cx36-ΔA14 were employed, and three images were captured across three separate experiments. One-way ANOVA with Tukey's statistical test was performed using IBM SPSS Statistics software. P value < 0.05 was considered statistically significant. HEK293T cells were obtained from ATCC (CRL-3216) and have been authenticated by the vendor. No further authentication was performed.

Reporting summary

Further information on research design is available in the Nature Portfolio Reporting Summary linked to this article.

Data availability

Fourteen cryo-EM density maps generated in this study have been deposited in Electron Microscopy Data Bank (EMDB) under accession codes EMD-38318 ($Cx36_{Nano-BL}$-WT in PLN state (D6 symmetry)), EMD-38346 ($Cx36_{Nano-BL}$-WT in PLN state (C1 symmetry)), EMD-38319 ($Cx36_{Nano-BL}$-WT in FN state (D6 symmetry)), EMD-38347 ($Cx36_{Nano-BL}$-WT in FN state (C1 symmetry)), EMD-38327 ($Cx36_{Nano-BL}$-MFQ (D6 symmetry)), EMD-38326 ($Cx36_{Nano-BL}$-MFQ (C1 symmetry)), EMD-38320 ($Cx36_{Nano-BL}$-AA (D6 symmetry)), EMD-38321 ($Cx36_{Nano-BL}$-AA (C1 symmetry)), EMD-38322 ($Cx36_{Nano-BL}$-Hexanol (D6 symmetry)), EMD-38323 ($Cx36_{Nano-BL}$-Hexanol (C1 symmetry)), EMD-38345 ($Cx36_{Nano-BL}$-ΔA14-MFQ (D6 symmetry)), EMD-38357 ($Cx36_{Nano-BL}$-ΔA14-MFQ (C1 symmetry)), EMD-38344 ($Cx36_{Nano-BL}$-ΔA14 (D6 symmetry)), and EMD-38356 ($Cx36_{Nano-BL}$-ΔA14 (C1 symmetry)). Seven atomic coordinates for models have been deposited at the Protein Data Bank (PDB) under accession codes 8XGD ($Cx36_{Nano-BL}$-WT in PLN state), 8XGE ($Cx36_{Nano-BL}$-WT in FN state), 8XGJ ($Cx36_{Nano-BL}$-MFQ), 8XGF ($Cx36_{Nano-BL}$-AA), 8XGG ($Cx36_{Nano-BL}$-Hexanol), 8XH9 ($Cx36_{Nano-BL}$-ΔA14-MFQ), and 8XH8 ($Cx36_{Nano-BL}$-ΔA14) (Supplementary Tables 2–4). The previously published structures used for structural comparison were obtained from the Protein Data Bank under accession codes 7XNH (Cx36), 7XKT (Cx36), 2ZW3 (Cx26), 6L3T (Cx31.3), 7F94 (Cx43), 7JKC (Cx46), and 7JJP (Cx50). Source data are provided with this paper.

References

1. Laird, D. W. & Lampe, P. D. Therapeutic strategies targeting connexins. *Nat. Rev. Drug Discov.* **17**, 905–921 (2018).
2. Brücher, B. L. & Jamall, I. S. Cell-cell communication in the tumor microenvironment, carcinogenesis, and anticancer treatment. *Cell. Physiol. Biochem.* **34**, 213–243 (2014).
3. Totland, M. Z. et al. Regulation of gap junction intercellular communication by connexin ubiquitination: physiological and pathophysiological implications. *Cell. Mol. Life Sci.* **77**, 573–591 (2020).
4. Bargiello, T. A. et al. Gating of Connexin Channels by transjunctional-voltage: conformations and models of open and closed states. *Biochim. Biophys. Acta* **1860**, 22–39 (2018).
5. Goodenough, D. A. & Paul, D. L. Beyond the gap: functions of unpaired connexon channels. *Nat. Rev. Mol. Cell Biol.* **4**, 285–295 (2003).
6. Rimkute, L. et al. Modulation of connexin-36 gap junction channels by intracellular pH and magnesium ions. *Front. Physiol.* **9**, 362 (2018).
7. Marandykina, A. et al. Regulation of connexin36 gap junction channels by n-alkanols and arachidonic acid. *J. Physiol.* **591**, 2087–2101 (2013).
8. Palacios-Prado, N. et al. Molecular determinants of magnesium-dependent synaptic plasticity at electrical synapses formed by connexin36. *Nat. Commun.* **5**, 1–13 (2014).
9. Ma, Y. et al. Analysis of the bystander effect in cone photoreceptors via a guided neural network platform. *Sci. Adv.* **4**, eaas9274 (2018).
10. Yamasaki, R. Connexins in health and disease. *Clin. Exp. Neuroimmunol.* **9**, 30–36 (2018).
11. Haefliger, J.-A. et al. Reduction of connexin36 content by ICER-1 contributes to insulin-secreting cells apoptosis induced by oxidized LDL particles. *PLoS One* **8**, e55198 (2013).
12. de Rivero Vaccari, J. C., Corriveau, R. A. & Belousov, A. B. Gap junctions are required for NMDA receptor–dependent cell death in developing neurons. *J. Neurophysiol.* **98**, 2878–2886 (2007).
13. Gajda, Z. et al. Quinine, a blocker of neuronal cx36 channels, suppresses seizure activity in rat neocortex in vivo. *Epilepsia* **46**, 1581–1591 (2005).
14. Juszczak, G. R. & Swiergiel, A. H. Properties of gap junction blockers and their behavioural, cognitive and electrophysiological effects:

animal and human studies. *Prog. Neuropsychopharmacol. Biol. Psychiatry* **33**, 181–198 (2009).
15. Wang, G. & Wu, X. The potential antiepileptogenic effect of neuronal Cx36 gap junction channel blockage. *Transl. Neurosci.* **12**, 46–51 (2021).
16. Shen, Y. et al. Secondary epileptogenesis: common to see, but possible to treat? *Front. Neurol.* **12**, 747372 (2021).
17. Lee, S.-N. et al. Cryo-EM structures of human Cx36/GJD2 neuronal gap junction channel. *Nat. Commun.* **14**, 1347 (2023).
18. Cruikshank, S. J. et al. Potent block of Cx36 and Cx50 gap junction channels by mefloquine. *Proc. Natl. Acad. Sci. USA* **101**, 12364–12369 (2004).
19. Beaumont, M. & Maccaferri, G. Is connexin36 critical for GABAergic hypersynchronization in the hippocampus? *J. Physiol.* **589**, 1663–1680 (2011).
20. Toovey, S. Mefloquine neurotoxicity: a literature review. *Travel Med. Infect. Dis.* **7**, 2–6 (2009).
21. Martins, A. C. et al. Review of the mechanism underlying mefloquine-induced neurotoxicity. *Crit. Rev. Toxicol.* **51**, 209–216 (2021).
22. Margineanu, D. G. & Klitgaard, H. The connexin 36 blockers quinine, quinidine and mefloquine inhibit cortical spreading depression in a rat neocortical slice model in vitro. *Brain Res. Bull.* **71**, 23–28 (2006).
23. Wang, Y. et al. Neuronal gap junctions are required for NMDA receptor–mediated excitotoxicity: Implications in ischemic stroke. *J. Neurophysiol.* **104**, 3551–3556 (2010).
24. Martin, F. C. & Handforth, A. Carbenoxolone and mefloquine suppress tremor in the harmaline mouse model of essential tremor. *Mov. Disord.* **21**, 1641–1649 (2006).
25. Shin, S. I. et al. Connexin-36 knock-out mice have increased threshold for kindled seizures: role of GABA inhibition. *Biochem. Pharmacol.* **9**, 2167–0501 (2013).
26. Wang, R. et al. Neonatal inhibition of connexin 36 ameliorates fetal brain injury induced by maternal noninfectious fever in mice. *Dev. Neurosci.* **41**, 94–101 (2019).
27. Voytenko, L. et al. Hippocampal GABAergic interneurons coexpressing alpha7-nicotinic receptors and connexin-36 are able to improve neuronal viability under oxygen–glucose deprivation. *Brain Res.* **1616**, 134–145 (2015).
28. Li, Q. et al. Connexin 36 mediates orofacial pain hypersensitivity through GluK2 and TRPA1. *Neurosci. Bull.* **36**, 1484–1499 (2020).
29. Manjarrez-Marmolejo, J. & Franco-Pérez, J. Gap junction blockers: an overview of their effects on induced seizures in animal models. *Curr. Neuropharmacol.* **14**, 759–771 (2016).
30. Marandykina, A. et al. The Effect of arachidonic acid on junctional conductance and gating of connexin 36 Gap junction channels and their modulation by N-alkanols. *Biophys. J.* **104**, 632a (2013).
31. Lavriha, P. et al. Mechanism of connexin channel inhibition by mefloquine and 2-aminoethoxydiphenyl borate. *bioRxiv*, https://www.biorxiv.org/content/10.1101/2023.12.11.571071v1 (2023).
32. Ding, X. et al. Structural basis of connexin-36 gap junction channel inhibition. *Cell Discov.* **10**, 68 (2023).
33. Burendei, B. et al. Cryo-EM structures of undocked innexin-6 hemichannels in phospholipids. *Sci. Adv.* **6**, eaax3157 (2020).
34. Kuzuya, M. et al. Structures of human pannexin-1 in nanodiscs reveal gating mediated by dynamic movement of the N terminus and phospholipids. *Sci. Signal.* **15**, eabg6941 (2022).
35. Lee, H.-J. et al. Conformational changes in the human Cx43/GJA1 gap junction channel visualized using cryo-EM. *Nat. Commun.* **14**, 1–18 (2023).
36. Syrjanen, J. L. et al. Structure and assembly of calcium homeostasis modulator proteins. *Nat. Struct. Mol. Biol.* **27**, 150–159 (2020).
37. Takahashi, H. et al. Cryo-EM structures of an LRRC8 chimera with native functional properties reveal heptameric assembly. *Elife* **12**, e82431 (2023).
38. Syrjanen, J. L. et al. On the molecular nature of large-pore channels. *J. Mol. Biol.* **433**, 166994 (2021).
39. Slater, S. J., Malinowski, S. A. & Stubbs, C. D. The nature of the hydrophobic n-alkanol binding site within the C1 domains of protein kinase Cα. *Biochemistry* **43**, 7601–7609 (2004).
40. Bukiya, A. N. et al. An alcohol-sensing site in the calcium-and voltage-gated, large conductance potassium (BK) channel. *Proc. Natl Acad. Sci. USA* **111**, 9313–9318 (2014).
41. Dhein, S. Gap junction channels in the cardiovascular system: pharmacological and physiological modulation. *Trends Pharmacol. Sci.* **19**, 229–241 (1998).
42. Moreno, A. P. et al. Biophysical evidence that connexin-36 forms functional gap junction channels between pancreatic mouse β-cells. *Am. J. Physiol. Endocrinol. Metab.* **288**, E948–E956 (2005).
43. Myers, J. B. et al. Structure of native lens connexin 46/50 intercellular channels by cryo-EM. *Nature* **564**, 372–377 (2018).
44. Nakase, T., Fushiki, S. & Naus, C. C. Astrocytic gap junctions composed of connexin 43 reduce apoptotic neuronal damage in cerebral ischemia. *Stroke* **34**, 1987–1993 (2003).
45. Paschon, V. et al. Blocking of connexin-mediated communication promotes neuroprotection during acute degeneration induced by mechanical trauma. *PLoS One* **7**, e45449 (2012).
46. Akopian, A. et al. Targeting neuronal gap junctions in mouse retina offers neuroprotection in glaucoma. *J. Clin. Investig.* **127**, 2647–2661 (2017).
47. Belousov, A. B. et al. A potential role for neuronal connexin 36 in the pathogenesis of amyotrophic lateral sclerosis. *Neurosci. Lett.* **666**, 1–4 (2018).
48. Schock, S. C. et al. ATP release by way of connexin 36 hemichannels mediates ischemic tolerance in vitro. *Biochem. Biophys. Res. Commun.* **368**, 138–144 (2008).
49. Fernández-Serra, R. et al. Postischemic neuroprotection of aminoethoxydiphenyl borate associates shortening of peri-infarct depolarizations. *Int. J. Mol. Sci.* **23**, 7449 (2022).
50. Flores, J. A. et al. Connexin-46/50 in a dynamic lipid environment resolved by CryoEM at 1.9 Å. *Nat. Commun.* **11**, 4331 (2020).
51. Hussain, N. et al. Cryo-EM structures of pannexin 1 and 3 reveal differences among pannexin isoforms. *Nat. Commun.* **15**, 2942 (2024).
52. Demura, K. et al. Cryo-EM structures of calcium homeostasis modulator channels in diverse oligomeric assemblies. *Sci. Adv.* **6**, eaba8105 (2020).
53. Syrjänen, J. L. et al. Structure of human CALHM1 reveals key locations for channel regulation and blockade by ruthenium red. *Nat. Commun.* **14**, 3821 (2023).
54. Kern, D. M. et al. Cryo-EM structures of the DCPIB-inhibited volume-regulated anion channel LRRC8A in lipid nanodiscs. *Elife* **8**, e42636 (2019).
55. Bukauskas, F. F. & Verselis, V. K. Gap junction channel gating. *Biochim. Biophys. Acta* **1662**, 42–60 (2004).
56. Nielsen, M. S. et al. Gap junctions. *Compr. Physiol.* **2** (2012).
57. Ghosh, D. K., Kumar, A. & Ranjan, A. Cellular targets of mefloquine. *Toxicology* **464**, 152995 (2021).
58. Srinivas, M., Hopperstad, M. G. & Spray, D. C. Quinine blocks specific gap junction channel subtypes. *Proc. Natl Acad. Sci. USA* **98**, 10942–10947 (2001).
59. Bargiello, T. A. et al. Voltage-dependent conformational changes in connexin channels. *Biochim. Biophys. Acta* **1818**, 1807–1822 (2012).
60. Kronengold, J. et al. Single-channel SCAM identifies pore-lining residues in the first extracellular loop and first transmembrane domains of Cx46 hemichannels. *J. Gen. Physiol.* **122**, 389–405 (2003).
61. Ek-Vitorin, J. F. & Burt, J. M. Structural basis for the selective permeability of channels made of communicating junction proteins. *Biochim. Biophys. Acta Biomembr.* **1828**, 51–68 (2013).

62. Ritchie, T. et al. Reconstitution of membrane proteins in phospholipid bilayer nanodiscs. *Methods Enzymol.* **464**, 211–231 (2009).
63. Punjani, A. et al. cryoSPARC: algorithms for rapid unsupervised cryo-EM structure determination. *Nat. Methods* **14**, 290–296 (2017).
64. Zivanov, J. et al. New tools for automated high-resolution cryo-EM structure determination in RELION-3. *Elife* **7**, e42166 (2018).
65. Emsley, P. & Cowtan, K. Coot: model-building tools for molecular graphics. *Acta Crystallogr. D.* **60**, 2126–2132 (2004).
66. Casañal, A., Lohkamp, B. & Emsley, P. Current developments in coot for macromolecular model building of electron cryo-microscopy and crystallographic data. *Protein Sci.* **29**, 1055–1064 (2020).
67. Afonine, P. V. et al. Real-space refinement in PHENIX for cryo-EM and crystallography. *Acta Crystallogr. D.* **74**, 531–544 (2018).
68. Pettersen, E. F. et al. UCSF Chimera—a visualization system for exploratory research and analysis. *J. Comput. Chem.* **25**, 1605–1612 (2004).
69. Pettersen, E. F. et al. UCSF ChimeraX: structure viscualization for researchers, educators, and developers. *Protein Sci.* **30**, 70–82 (2021).
70. El-Fouly, M. H. et al. Scrape-loading and dye transfer: a rapid and simple technique to study gap junctional intercellular communication. *Exp. Cell Res.* **168**, 422–430 (1987).
71. Schneider, C. A. et al. NIH Image to ImageJ: 25 years of image analysis. *Nat. Methods* **9**, 671–675 (2012).
72. Dydowiczová, A. et al. Improved multiparametric scrape loading-dye transfer assay for a simultaneous high-throughput analysis of gap junctional intercellular communication, cell density and viability. *Sci. Rep.* **10**, 730 (2020).

Acknowledgements

We thank Prof. Jae-Sung Woo (Korea University, South Korea), Prof. Insuk So (Seoul National University, South Korea), and Dr. Jinsung Kim (Seoul National University, South Korea) for extensive discussion. The cryo-EM experiments were performed at the PNU CORE research facilities of Pusan National University, Center for Macromolecular and Cell Imaging of Seoul National University, National Center for Inter-University Research Facilities (NCIRF) of Seoul National University, Korea Basic Science Institute (KBSI), Institute for Basic Science (IBS), Bio Open Innovation Center (BOIC) of Pohang University of Science and Technology, and Institute of Membrane Proteins (IMP). This work was supported by Samsung Science & Technology Foundation and Research (SSTF-BA2101-13).

Author contributions

H.J.C. and H.H.L. conceived this project. H.J.C. performed all the experiments and D.K.C. performed the SL-DT experiments during the revision. H.J.C. and H.H.L. analyzed the data and wrote the manuscript and H.H.L. directed the work.

Competing interests

The authors declare no competing interests.

Additional information

Supplementary information The online version contains supplementary material available at https://doi.org/10.1038/s41467-024-53587-6.

Correspondence and requests for materials should be addressed to Hyung Ho Lee.

Peer review information *Nature Communications* thanks the anonymous reviewer(s) for their contribution to the peer review of this work. A peer review file is available.